Materials Advances

ROYAL SOCIETY OF CHEMISTRY

PAPER

View Article Online
View Journal | View Issue

Cite this: *Mater. Adv.*, 2025, 6, 3495

Potential of biodegradable Zn alloys with fine grains for orthopedic and antibacterial applications

Haifeng Liang,†[a] Haoran Wu,†[b] Delong Yin,†[a] Hui Yu,[a] Zhuoxuan He,[a] Wenqian Zhang,[a] Zerong Wang,[a] Tuquan Zheng,[a] Xiaochuan Li,*[c] Yu Cai*[a] and Guiyong Jiang *[d]

Zinc (Zn) alloys with high elongation have attracted significant attention in biomedical applications. These alloys possess fine-grained microstructures that greatly influence their corrosion behavior and biocompatibility. In this study, a minor addition of Cu decreased the average grain size from 17.36 μm in pure Zn to 2.15 μm in the Zn-0.4Cu alloy after equal channel angular pressing (ECAP). Results demonstrated that grain refinement enhanced elongation to 200% by altering the deformation mechanism. The deformation mode of pure Zn was dominated by twin-induced dynamic recrystallization (T-DRX), while that of the Zn-0.4Cu alloy was characterized by dislocation slip and grain boundary sliding. Furthermore, grain refinement led to a decrease in corrosion rate from 270.72 ± 9.76 μm per year to 186.34 ± 8.63 μm per year, which was attributed to a shift in corrosion mode from pitting corrosion to grain boundary corrosion. The occurrence of grain boundary corrosion was due to Cu enrichment near the grain boundaries, which accelerated corrosion *via* galvanic effects. Both pure Zn and Zn–Cu alloys demonstrated excellent biocompatibility with endothelial cells and bone marrow stem cells. The reduced concentration of Zn^{2+} ions promoted the osteogenic properties of Zn-0.4Cu alloys *via* grain refinement. Moreover, the release of Cu^{2+} ions improved the antibacterial properties. These findings offer valuable insights into the impact of grain refinement on the mechanical properties and corrosion behavior of biodegradable Zn alloys.

Received 1st November 2024,
Accepted 12th April 2025

DOI: 10.1039/d4ma01094a

rsc.li/materials-advances

Introduction

Zinc (Zn) has emerged as a new class of biodegradable metal, following magnesium (Mg) and iron (Fe), due to its suitable *in vivo* degradation rate and excellent biocompatibility.[1,2] Additionally, Zn has a low melting point and a dynamic recrystallization (DRX) temperature close to room temperature, enabling some Zn alloys to undergo plastic processing under ambient conditions.[3,4] Room-temperature processing is beneficial for grain refinement by mitigating the growth of DRX grains. It has been reported that some Zn alloys can be plastically deformed at room temperature.[5–9] The grain sizes of these Zn alloys are often refined to the micrometer or even sub-micrometer scale after plastic deformation at room temperature.[10] This refinement significantly enhances the mechanical properties of Zn alloys, particularly their elongation. Zn–Cu alloys are particularly notable for their exceptional elongation. For instance, as-rolled Zn–1Cu alloys with an average grain size of 1.3 μm can achieve elongations exceeding 450% at a strain rate of 10^{-4} s^{-1}.[9] In the biomedical field, some complex devices, such as stents, require high elongation, which is an advantage of Zn–Cu alloys.[11,12] Moreover, Zn–Cu alloys can be rolled into thin plates, which are beneficial for preparing guided bone regeneration (GBR) membranes.[13–17] These studies demonstrate that Zn–Cu alloys with high elongation have great potential for the development of complex biomedical devices.

Apart from mechanical properties, corrosion rates are also important for biodegradable Zn alloys. Biodegradable metals should degrade at a corrosion rate of <0.2 mm per year to maintain mechanical integrity.[18,19] The corrosion rates of Zn

[a] *Department of Orthopaedic Surgery, Guangzhou Key Laboratory of Spine Disease Prevention and Treatment, Guangdong Provincial Key Laboratory of Major Obstetric Diseases, Guangdong Provincial Clinical Research Center for Obstetrics and Gynecology, The Third Affiliated Hospital, Guangzhou Medical University, Guangzhou, 511495, China. E-mail: 1215237994@qq.com*
[b] *Institute of Materials, Henan Academy of Sciences, Zhengzhou 450046, China*
[c] *Department of Orthopedic Surgery, Gaozhou People's Hospital, No. 89 XiGuan Rd, Gaozhou 525200, China. E-mail: lixcgzph@163.com*
[d] *Division of Orthopaedics and Traumatology, Department of Orthopaedics, Nanfang Hospital, Southern Medical University, Guangzhou, 510515, China. E-mail: nfyy_jgy@163.com*
† These authors contributed equally to this work.

alloys are affected by the formation of second phases and grain size. Excess alloying elements beyond their solid solubility inevitably form second phases, which promote galvanic corrosion due to the potential difference between them and the Zn matrix. However, second phases are absent from microstructures when the alloying elements are completely dissolved in the Zn matrix or segregated at the grain boundary. Studies on the corrosion behavior of Zn–Cu alloys have shown that increasing the Cu content accelerates corrosion, which is attributed to the formation of $CuZn_5$ phases.[20] Such accelerated corrosion promotes the release of Cu ions, resulting in an increase in the Cu ion concentration.[21] The recommended daily intake of Cu for adults is 0.6 mg, which is far lower than the 15 mg of Zn.[22] It is therefore important to decrease the Cu content in Zn–Cu alloys to avoid excess Cu toxicity. However, traditional processes, such as extrusion and rolling, have limited effects on the grain refinement of Zn–Cu with a low Cu concentration.[6] Therefore, selecting an appropriate process is necessary for refining the grains of Zn–Cu alloys to ensure the absence of $CuZn_5$ phases.

Equal channel angular pressing (ECAP) is a common method to fabricate fine-grained and ultrafine-grained metals.[23] Previous studies have demonstrated that Zn–0.5Cu alloys have an average grain size of 1.02 μm after ECAP.[5] With increasing the Cu content, the average grain size of Zn–1Cu and Zn–2Cu alloys were found to be 5.4 and 1.27 μm, respectively.[24,25] Thus, a minor addition of Cu is able to significantly refine the grains of Zn alloys *via* ECAP. However, while it was found that the $CuZn_5$ phases were absent from the microstructures of Zn–0.5Cu alloys at the microscale level, nanosized precipitates (<100 nm) were founds to be present in the grains.[26] Reducing the Cu concentration to below 0.5 wt% could help to continuously decrease the fraction of these nanosized precipitates. In previous studies, Zn–0.5Cu alloys after ECAP have exhibited room-temperature superplasticity due to their refined grains. However, the role of grain refinement in the corrosion behavior and biocompatibility of Zn–Cu alloys with a low Cu content remains underexplored.

In this study, we selected a Zn-0.4Cu alloy that contained less nanosized precipitates as the research object. After ECAP, the Zn-0.4Cu alloys achieved fine grains (2.15 μm) and high room-temperature elongation (>200%). Electrochemical and immersion experiments were conducted to compare the corrosion modes of the Zn–Cu alloys and pure Zn, also for revealing the mechanisms behind the improved corrosion resistance of the Zn–Cu alloys. Finally, we evaluated the biological functions of Zn–Cu alloys to establish their biocompatibility, which could reinforce their potential in the field of biodegradable metals.

Experimental section

Preparation and characterization of pure Zn and Zn–Cu alloys

Zn-0.4Cu wt% alloy, with an actual composition of Zn–0.39Cu wt%, was fabricated from high-purity Zn (99.99 wt%) and Cu (99.95 wt%) metals. Following melting in a low-carbon steel crucible under a mixed gas environment of CO_2 and SF_6 (99 : 1 ratio), the molten alloy was cast into a copper mold with dimensions of 200 mm × 50 mm × 50 mm. Samples with a cubic shape, measuring 45 × 20 × 20 mm, were extracted from the ingot for ECAP. ECAP was executed at ambient temperature, with a pass setting of 12.

Scanning electron microscopy (SEM) was employed to analyze the microstructures of the pure Zn and Zn–Cu alloys. An energy-dispersive X-ray spectroscopy (EDS) system, specifically the GENESIS 60S model, equipped with SEM, was utilized to assess the elemental distributions of the pure Zn and Zn alloys. Prior to microstructure examination, the alloy surfaces underwent mechanical grinding, polishing, and etching. The etching solution consisted of 4 wt% nitric acid in alcohol. To delve deeper into the microstructural changes occurring before and after the tensile testing, electron backscatter diffraction (EBSD) and transmission electron microscopy (TEM) were performed. The EBSD samples were prepared through mechanical grinding followed by electrochemical polishing using a 10 vol% $HClO_4$ solution, with the polishing parameters set at −30 °C and 15 V. For TEM, the samples were prepared using twin-jet electron polishing in a solution of 4 wt% perchloric acid in alcohol.

Tensile tests

Standard tensile dog-bone specimens were sectioned along the ECAP direction *via* electrical discharge machining (EDM). Prior to testing, all the specimens underwent mechanical grinding. Tensile testing was executed on a universal material testing machine (Zwick/Roell Z100, Germany). The gauge length was set at 10 mm, and a strain rate of 1×10^{-3} s^{-1} was chosen for the tests. Furthermore, to explore the microstructural evolutions, fractured specimens were prepared for EBSD analysis.

Electrochemical and immersion tests

The electrochemical tests were carried out on a CHI660C electrochemical workstation, which was equipped with a traditional three-electrode setup within an electrochemical cell.[27,28] Initially, the electrochemical specimens were ground using SiC papers with grits ranging from 400 to 2000, and then polished with a diamond suspension. The exposed surface area of the samples in simulated body fluid (SBF) was 10 × 10 mm, and testing was conducted at a temperature of 37 °C. After placing the working electrode in the SBF solution, potentiodynamic polarization (PDP) curves were obtained by sweeping the potential from −1.6 V (*vs.* SCE) to −0.5 V (*vs.* SCE) at a scan speed of 0.1 mV s^{-1}. The self-corrosion potential and corrosion current density (i_{corr}) were derived from the PDP curves. Prior to the immersion tests, all the specimens were subjected to mechanical grinding and polishing. The processed samples were then placed into centrifuge tubes filled with SBF solution. The ratio of the exposed metal area to the solution volume was maintained at 20 mL cm^{-2}. After a 30-day immersion, the specimens were removed from the SBF solution and rinsed with deionized water. The corrosion products on the sample surfaces were eliminated using 200 g L^{-1} chromic acid solution. The corrosion rate (C, μm per year) was calculated

using the equation: $C = \Delta m/\rho At$, where Δm is the weight loss (mg), ρ is the density (g cm^{-3}), A is the exposed area (cm^2), and t is the time (years).

Cell viability tests

Endothelial cells (ECs, Cell Bank, Chinese Academy of Sciences, catalog no. CP-H082) and bone mesenchymal stem cells (BMSCs, Cell Bank, Chinese Academy of Sciences, catalog no. CP-H166) were cultured in Dulbecco's modified Eagle's medium (DMEM, Gibco) containing 10% fetal bovine serum (FBS) at 37 °C and 5% CO_2. Cell viability was assessed using the Cell Counting Kit-8 (CCK-8) through an indirect contact method. The disc samples for the cytotoxicity analysis were prepared in the same way as those used in the immersion tests. In line with ISO 10993-12:2012, extracts from the pure Zn and the Zn-0.4Cu alloy were created by immersing the disc samples with an exposed area of 2.2 cm^2 in DMEM for 72 h. The surface area to medium volume ratio was set to 1.25 cm^2 mL^{-1}. The extracts were diluted to 50% concentration for subsequent testing. The ion concentrations within the extracts were measured using inductively coupled plasma-mass spectrometry (ICP-MS, Thermo Fisher, USA). The test cells were plated in to 96-well plates at 2000 cells per well. Following 24-h incubation to promote cell attachment, the medium was replaced with diluted sample extracts. The cells were then incubated for 3 days, after which 10 μL of CCK-8 solution was added to each well. The absorbance was measured after a 2-h incubation, using a microplate reader (iMARK, Bio-Rad, USA) at 450 nm wavelength. The concentrations of the pure Zn and Zn-0.4Cu alloy extracts were measured by inductively coupled plasma-mass spectrometry (ICP-MS, Agilent 7700, USA).

Live/dead staining was applied to further test the cytotoxicity of the alloy extracts. ECs and BMSCs were seeded in to 96-well plates, respectively, and then the pure Zn or Zn–Cu alloy extract and PBS buffer were added for co-culturing for 24 h. After this incubation, the cells were washed with PBS to remove any unbound extracts. Calcein AM (1 μM, Thermo Fisher, USA) and PI (2 μg mL^{-1}, Thermo Fisher, USA) dyes in the corresponding proportions were then added and the cells were incubated again for 15 min at room temperature. After staining was completed, cell viability and death were observed using a fluorescence microscope (Olympus Co., Ltd, Tokyo, Japan).

Osteogenesis-induction tests

BMSCs were seeded in to 6-well plates at a density of 6×10^4 per well. When the cell fusion reached 80%, the medium was replaced with osteogenic induction medium containing 50% extract, and was replaced every 48 h. The BMSCs were stained with alkaline phosphatase (ALP) and alizarin red S (ARS) on day 7 and day 14 during culture. After staining was completed, the staining results were observed and recorded using a optical microscope (Olympus Co., Ltd, Tokyo, Japan).

Also, BMSCs were seeded on the coverslips of a 24-well plate at a density of 5000 per well. When the cell fusion reached 80%, the medium was replaced with osteogenic induction medium containing 50% extract. After 7 days, the BMSCs were washed with PBS buffer, then fixed with 4% paraformaldehyde for 15 min, then permeabilized with 0.1% Triton X-100 for 10 min, then blocked with 10% BSA for 1 h, and finally a specific primary antibody to Runx2 (1:200 dilution, ab192256, abcam, USA) was added and the cells were incubated at 4 °C overnight. The next day, after washing the cells with PBS three times, fluorescently labeled secondary antibodies (diluted 1:500, abcam, USA) were added followed by incubation for 1 h at room temperature. Finally, the cytoskeletons and nuclei were stained with FITC-phalloidin and DAPI (Sigma-Aldrich, USA), and the expression of Runx2 was observed and recorded under a confocal microscope (ZEISS, Germany).

Further, the BMSCs were seeded in to 6-well plates at a density of 6×10^4 per well. When the cell fusion reached 80%, the medium was replaced with osteogenic induction medium containing 50% extract and the culture was continued for 10 days. After the culture, the total RNA was extracted using the RNeasy Mini Kit (Qiagen), and the RNA concentration and purity were determined. Here, 1 μg of RNA was extracted from each group and cDNA was synthesized using the Super Script™ III Reverse Transcription Kit (Thermo Fisher, USA). The reverse transcription reaction conditions were: annealing at 65 °C for 5 min, 4 °C for 1 min, reverse transcription at 50 °C for 60 min, and then the reaction was terminated at 70 °C for 15 min. Real-time PCR was used using the SYBR Premix Ex TaqII (2X) system (Takara, Japan). The qPCR reaction conditions were: pre-denaturation at 95 °C for 30 s; followed by 40 cycles, each cycle was denatured at 95 °C for 5 s, followed by annealing and extension at 60 °C for 30 s. The expressions of the osteogenesis-related genes Runx2, OPN, and COL1 were detected by qPCR, with GAPDH as the internal reference gene. Gene expression analysis was performed using a real-time fluorescence quantitative PCR instrument (Thermo Fisher, USA), and relative expression was calculated by the ΔΔCt method.

Antibacterial tests

The antibacterial activity of the pure Zn and Zn–Cu alloys against *Staphylococcus aureus* (*S. aureus*, ATCC 6538) and *Escherichia coli* (*E. coli*, ATCC 25922) was evaluated using the spread plate and crystal violet assay methods. Pure Ti was used as the control group. *S. aureus* and *E. coli* were cultured in tryptone soy broth (TSB) medium for 24 h at 37 °C, with shaking at 150 rpm in Luria–Bertani (LB) broth. The cultures were subsequently grown for 3 to 5 generations on LB agar plates at 37 °C in an incubator. Bacterial suspensions (5×10^7 CFU mL^{-1}) were diluted to 1 mL and added to each well. A 100-fold dilution of the PBS solution was spread on the LB agar plates, followed by incubation at 37 °C for 24 h. The antibacterial rate (AR) was calculated using the equation: $AR = [(N_c - N_s)/N_c] \times 100\%$, where N_c represents the average colony count on pure Ti, and N_s represents that on the pure Zn and Zn–Cu alloy plates.

To assess the ability of the pure Zn and Zn–Cu alloys to inhibit biofilm formation on plastic instruments, samples were first placed at the bottom of well plates. Bacteria (*S. aureus* or *E. coli*) were inoculated in a 24-well plate at a density of 5×10^7 CFU mL^{-1}, with equal amounts of pure Zn, Zn–Cu alloy extract and PBS buffer per well. After 24 h of incubation, each

well was washed with PBS to remove free bacteria. Subsequently, crystal violet solution (0.25%) was added to stain the cells, which were incubated at room temperature for 15 min. After dyeing was complete, the cells were washed with PBS to remove any unbound dye, and then ethanol was added to dissolve the crystal violet. Absorbance was then measured using a microplate reader (iMARK, Bio-Rad, USA) at a wavelength of 600 nm.

Statistical analysis

The statistical significance of the differences between groups was analyzed using one-way analysis of variance (ANOVA) followed by Turkey *post hoc* tests. Data were expressed as the mean ± standard deviation (SD). Differences of $*p < 0.05$, $**p < 0.01$, $*p < 0.001$, and $****p < 0.0001$ were considered statistically significant and statistically highly significant, respectively.

Results

Microstructures

Fig. 1 presents the microstructures of the pure Zn and Zn-0.4Cu alloy. XRD analysis confirmed the single-phased microstructures in all the samples, attributed to the high solid solubility of Cu in Zn.[29] Upon Cu addition, the intensity of the basal planes decreased significantly, while that of the prismatic and pyramidal planes increased, indicating that Cu plays a key role in influencing the orientation of Zn grains. SEM images (Fig. 1(b)) further confirmed the single-phased microstructures, showing only Zn grains of varying sizes. Next, EBSD analysis was used to study the effect of Cu on the orientations and sizes of the grains. The inverse pole figures (IPFs) showed that the average grain size of pure Zn decreased from 17.36 μm to 2.15 μm after a minor addition of Cu. Meanwhile, the fraction of Zn grains with a basal orientation, which is represented by the red color

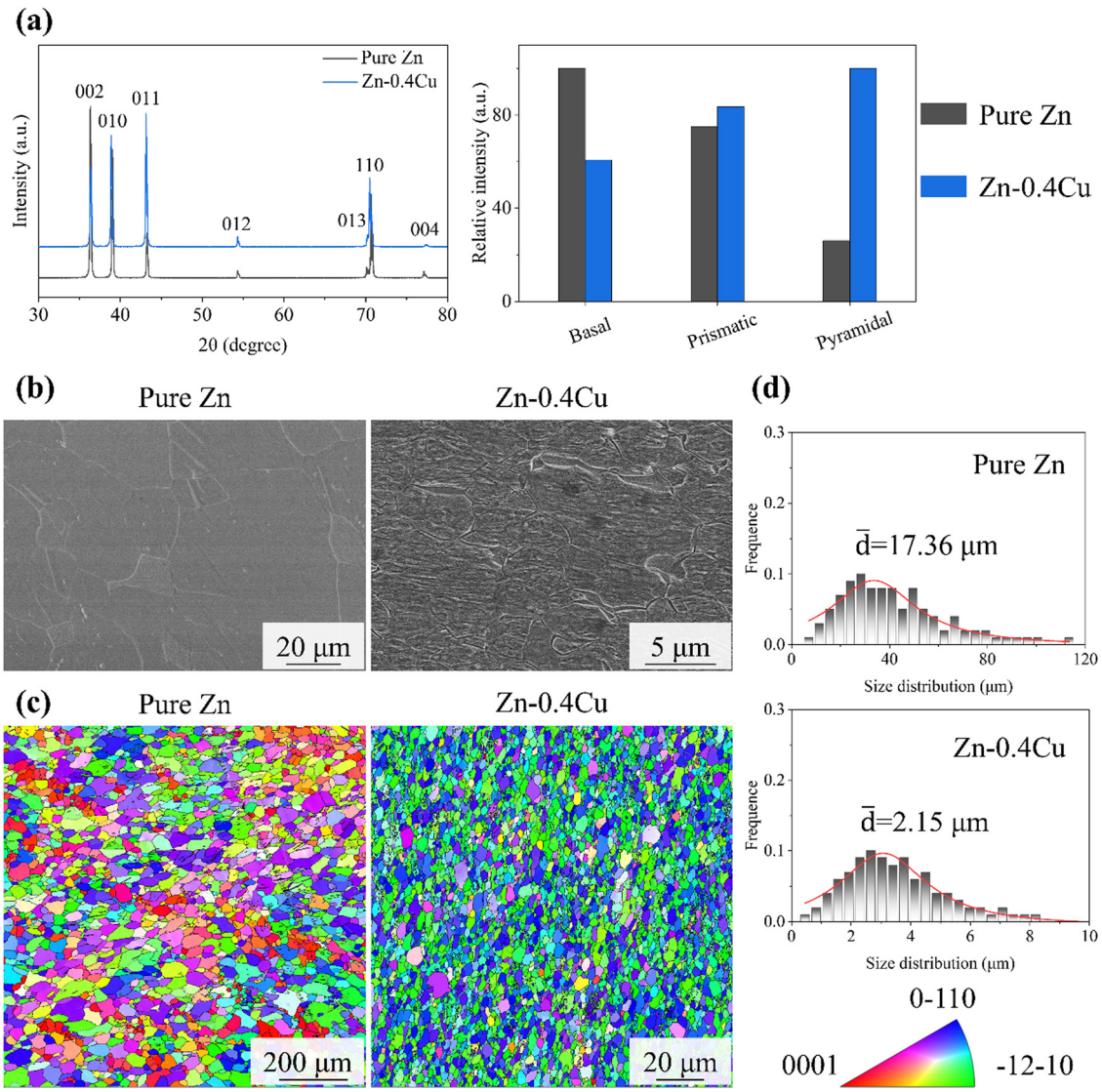

Fig. 1 Microstructures of pure Zn and Zn alloy: (a) XRD spectra and relative intensity of the various planes. (b) SEM images. (c) IPF mappings and average grain sizes. (d) Grain size distributions.

in the figures, decreased while those of the grains with prismatic and pyramidal orientations increased. This result was consistent with the XRD analysis.

Fig. 2 presents the microstructures analyzed by EBSD. After plastic deformation, a significant increase in dislocations within the grains was observed. Next, Kernel average misorientation (KAM) mapping was used to assess the dislocation density, which leads to a local misorientation. In the KAM mappings (Fig. 2(a)), the green regions represent areas of high misorientation. The dislocation density (ρ) was calculated using the relationship: $\rho = \frac{2\theta}{\mu b}$, where ρ, θ, μ, and b are the dislocation density, KAM value, step size, and Burgers vector, respectively. The average KAM values for the pure Zn and Zn-0.4Cu alloy were 0.37° and 0.5°, corresponding to dislocation densities of 0.63×10^{14} and 5.12×10^{14} m^{-2}, respectively.

The pole figures indicated that the texture direction in pure Zn was parallel to the basal plane, while in the Zn-0.4Cu alloy, it was perpendicular to the basal plane. The Schmid factor (SF), which is related to the deformation ability, is given by the expression: $\tau = \sigma \cdot m$, where τ is the critical resolved shear stress, σ is the principal stress, and m is the SF value. A high SF value indicates that the deformation modes are more easily activated. In pure Zn, both the dislocation slip and twinning deformation had SF values exceeding 0.3, with the basal $\langle \mathbf{a} \rangle$, $\langle \mathbf{c} + \mathbf{a} \rangle$ dislocation slip, and twinning deformation being the dominant deformation modes.

TEM was used to further examine the microstructures of the Zn–Cu alloy, as shown in Fig. 3. Fine grains, ranging from 1 to 3 μm in size, were observed in Fig. 3(a). Additionally, a significant number of precipitates were detected within certain grains. The presence of additional diffraction spots in the selected area electron diffraction (SAED) images indicated that these precipitates were oriented with respect to the Zn matrix. EDS mapping confirmed that the precipitates were rich in Cu and exhibited a coherent interface with the Zn matrix (Fig. 3(e)). Besides the precipitates, Cu was also concentrated at the grain boundaries, forming a double-layer structure with the Cu-rich regions. The spacing between these layers was approximately 3 nm. In summary, TEM analysis revealed that the Cu in the Zn–Cu alloys was distributed within the grain interiors as a solid solution and precipitates, and was segregated at the grain boundaries.

Mechanical behaviors

Fig. 4(a) presents the engineering stress–strain curves. The ultimate tensile strength (UTS) increased from 90 MPa in pure Zn to 130 MPa in the Zn-0.4Cu alloy. At the same time, the elongation was improved from 90% in pure Zn to 200% in Zn-0.4Cu, indicating room-temperature superplasticity. The microstructure of the fractured samples was analyzed using EBSD. The IPF mappings revealed that the average grain size of the fractured pure Zn decreased significantly, from 17.36 μm to 4.08 μm, while the grain size of the fractured Zn-0.4Cu alloy remained nearly unchanged.

Grain refinement in pure Zn was associated with DRX, which could be characterized by the grain orientation spread (GOS) values. The blue regions in the GOS maps correspond to lower GOS values, indicating the lower local strain in the DRX grains. Grains with a GOS value below 1° were identified as DRX

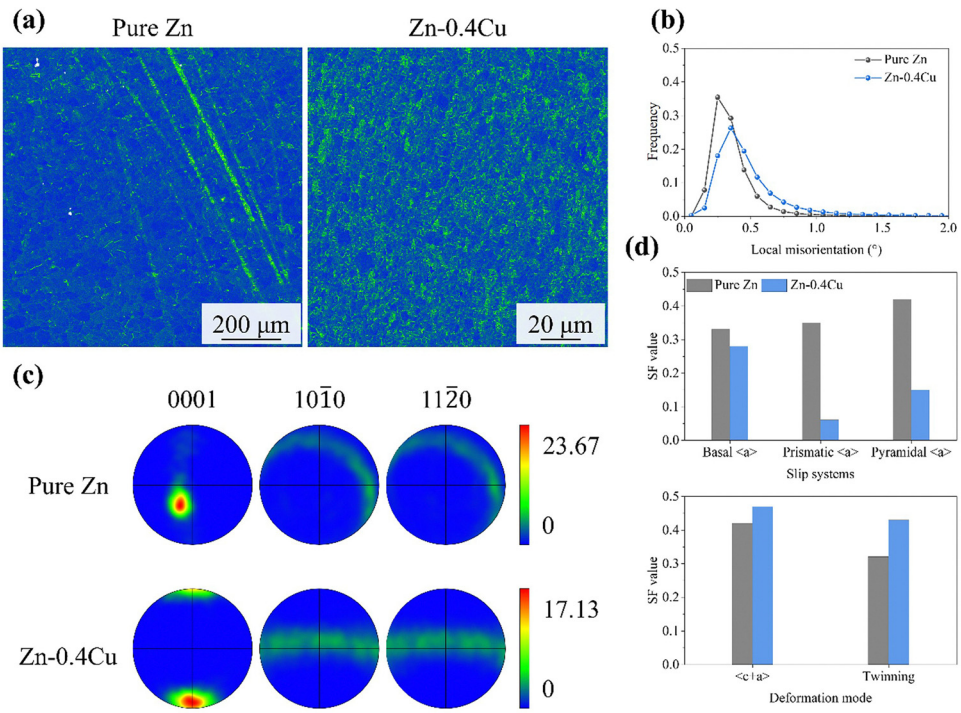

Fig. 2 Microstructural analysis by EBSD: (a) LAM mappings. (b) Distributions of local misorientation. (c) Textures. (d) SF values of different deformation modes.

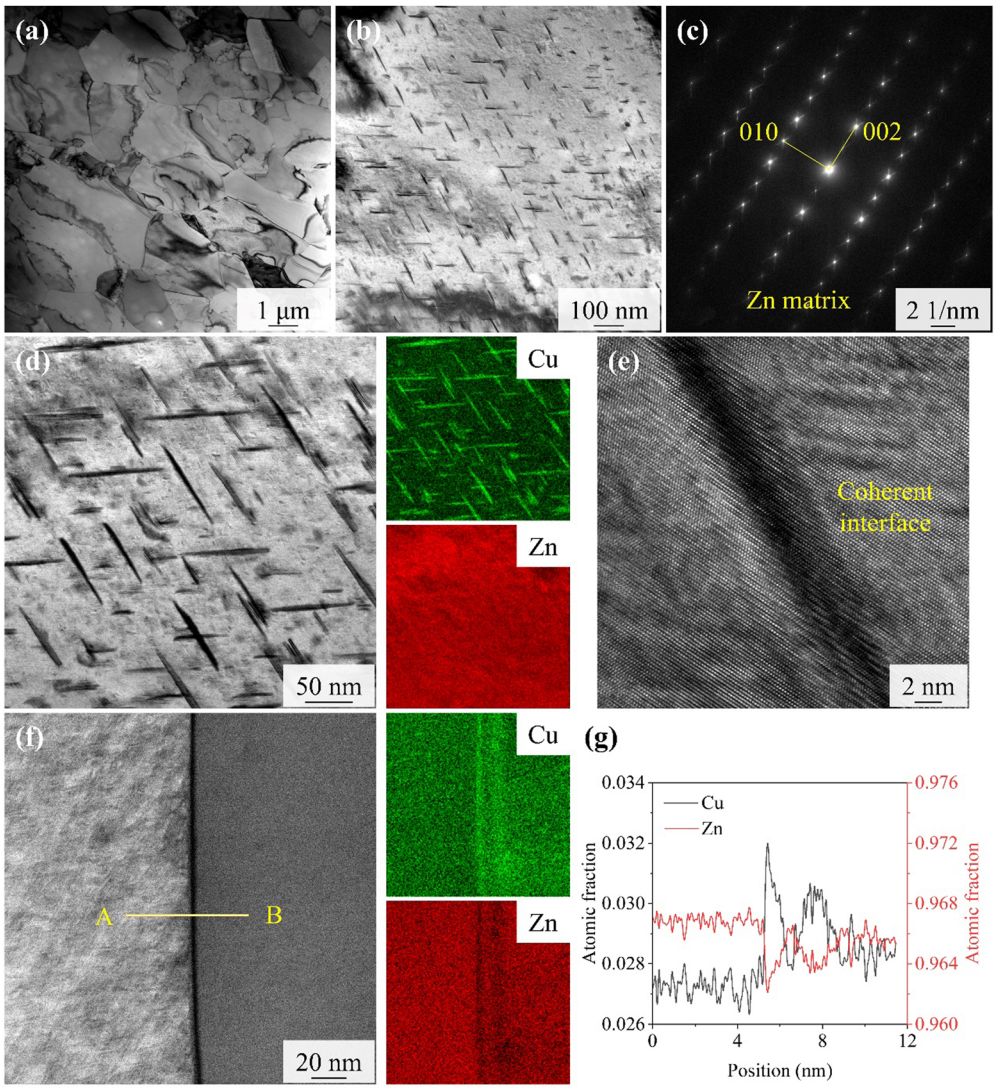

Fig. 3 TEM images of the Zn-0.4Cu alloy: (a) grain regions. (b) Plate-shaped precipitates. (c) SAED image. (d) Precipitates and the corresponding element distributions. (e) HR-TEM image of precipitates. (f) Grain boundary and the corresponding element distributions. (g) Atomic fractions of Zn and Cu.

grains, and the proportion of DRX grains in the fractured pure Zn was 40%, compared to only 10% in the fractured Zn-0.4Cu alloy.

Fig. 4(c) shows the misorientation distributions. After fracture, the proportion of low-angle grain boundaries decreased, while the proportion of twin boundaries increased in pure Zn. In the Zn-0.4Cu alloy, both the low-angle grain boundaries and twin grain boundaries slightly increased after fracture. The texture analysis showed that the texture type of the fractured Zn-0.4Cu alloy was similar to that of pure Zn, though the texture intensity was slightly higher, which may be attributed to the increase in the low-angle grain boundaries.

Corrosion behaviors

Fig. 5 illustrates the electrochemical corrosion behaviors of the pure Zn and the Zn-0.4Cu alloy. Here, E_{corr} and i_{corr} can be used to assess the corrosion resistance from the thermodynamics and kinetics, respectively. The two parameters were derived from the PDP curves in Fig. 5(a) by a linear extrapolation method within the cathodic curves. As shown in Table 1, E_{corr} increased from −1.22 V *vs.* SCE for pure Zn to −1.17 V *vs.* SCE for the Zn-0.4Cu alloy, while i_{corr} decreased from 10.83 μA cm^{-2} to 6.78 μA cm^{-2}. This indicated that the Zn-0.4Cu alloys had a better corrosion resistance than the pure Zn. Moreover, immersion experiments were also performed and demonstrated that the corrosion rates decreased from 270.72 ± 9.76 μm per year for pure Zn to 186.34 ± 8.63 μm per year for the Zn-0.4Cu alloy. The low corrosion rates indicated that the Zn^{2+} concentration decreased from 3.13 ± 0.58 mg L^{-1} to 1.62 ± 0.49 mg L^{-1}. A slight amount of Cu^{2+} was also detected and its concentration was 14.31 ± 2.97 μg L^{-1}.

Fig. 5(b) displays the Nyquist plots of the pure Zn and Zn-0.4Cu alloy in the medium-to-low-frequency range. It was evidenced that the Nyquist plots were composed of two capacitive loops by fitting with an equivalent circuit (see the inset in Fig. 5(b)). The diameter of the capacitive loops for the Zn-0.4Cu

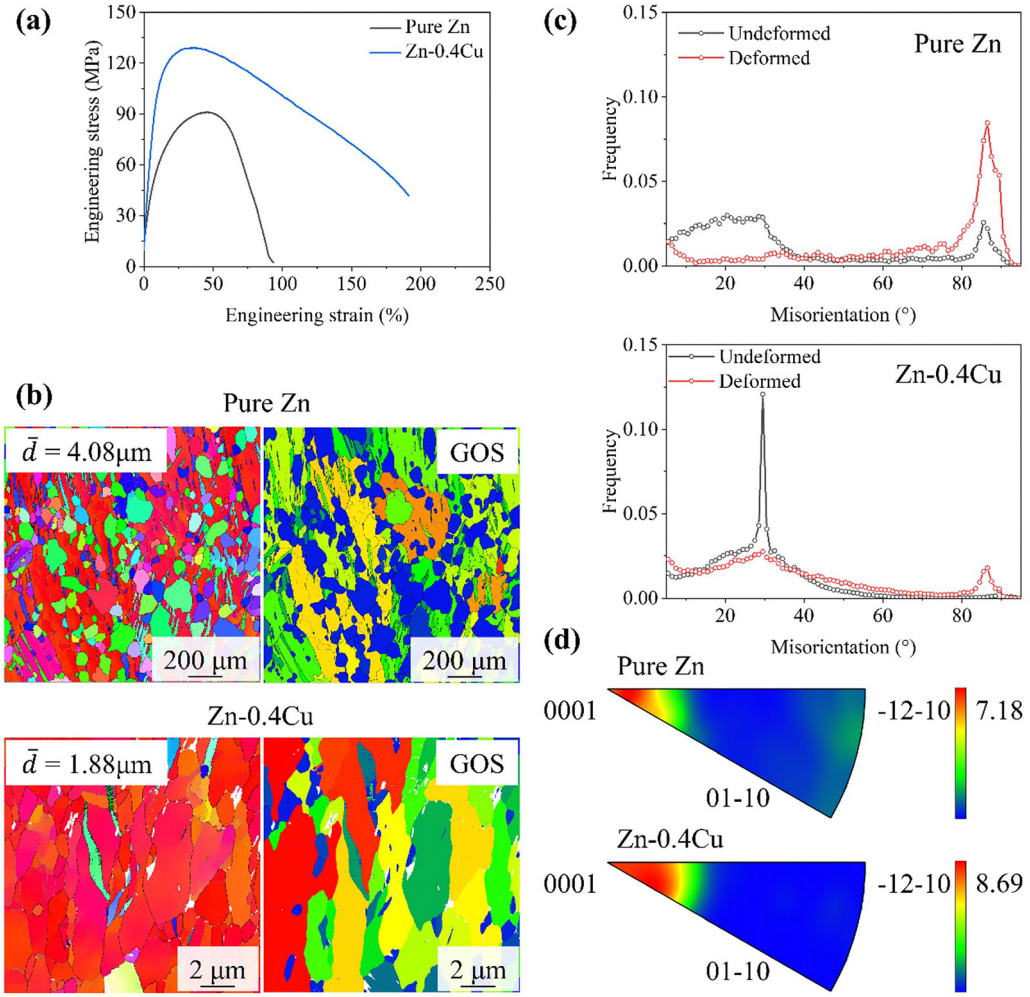

Fig. 4 Mechanical behaviors of the samples: (a) typical tensile curves. (b) IPF and GOS mappings. (c) Misorientations. (d) IPF textures.

alloy was larger than that for pure Zn, indicating its better corrosion resistance. The improved resistance was attributed to the formation of a surface oxide layer that induced charge-transfer resistance between the specimen and SBF solution. The charge-transfer resistance includes mass transport in the solid phase and ion diffusion through the oxide layer. The former was reflected by the loop in the medium-frequency range while the latter was assigned to the loop in the low-frequency range.[30,31] It was demonstrated that the charge-transfer resistance (R_{ct}) of pure Zn was 1.9 kΩ cm^2, which was lower than the 3.3 kΩ cm^2 of the Zn-0.4Cu alloy, as shown in Table 2. Moreover, Bode diagrams were expressed in the form of absolute impedance (Fig. 5(c)) and phase angle distribution (Fig. 5(d)). It was found that the absolute impedance ($|Z|$) of the Zn-0.4Cu alloy was higher than that of pure Zn in the medium- and low-frequency ranges, indicating a higher impedance. The maximum phase angle of the Zn-0.4Cu alloy was 63°, which was higher than the 53° of pure Zn. The higher phase angle indicated the existence of a compact corrosion layer.[32]

Fig. 6 displays the surface morphologies of the pure Zn and Zn-0.4Cu alloy after immersion for 30 days. Both samples exhibited a substantial accumulation of corrosion products on their surfaces. In pure Zn, these corrosion products appeared as particles of varying sizes. The EDS mapping indicated that these particles were rich in oxygen (O) and phosphorus (P). In contrast, the corrosion products on the Zn-0.4Cu alloy displayed different morphologies; whereby in addition to small white particles, deep-contrast regions were observed. The EDS mapping also revealed a concentration of carbon (C) in these areas. XRD and XPS analyses were used to further identify the corrosion products, confirming the presence of C, O, Ca, P, and Zn. After removing the corrosion products, the exposed surfaces were analyzed (Fig. 6(d)). A significant number of corrosion pits were noted on the surface of pure Zn, with sizes ranging from a few micrometers to several micrometers. In the Zn-0.4Cu alloy, corrosion cracks were observed along the grain boundaries. In summary, the corrosion mode in pure Zn was characterized by pitting corrosion, while grain boundary corrosion predominated in the Zn-0.4Cu alloy.

To further determine the composition of the corrosion products, Fig. 7 presents the high-resolution spectra of various elements. The C 1s spectrum exhibited two binding energy peaks at 284.5 and 286 eV, which corresponded to metallic

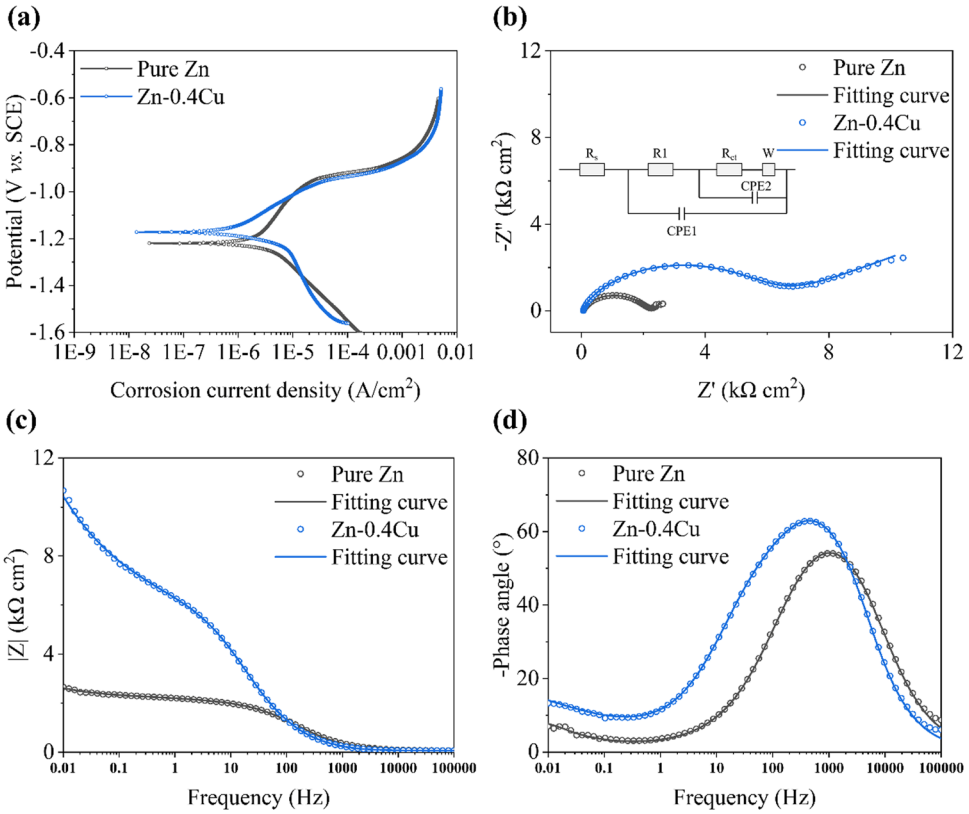

Fig. 5 Electrochemical behavior of the samples: (a) PDP curves. (b) Nyquist plots and fitting curves (inert image shows the fitting circuit). (c) |*Z*| and (d) -phase angle *vs.* frequency.

Table 1 Electrochemical parameters, ionic concentrations, and corrosion rates of pure Zn and Zn-0.4Cu alloy

Samples	i_{corr} (μA cm^{-2})	E_{corr} (V *vs.* SCE)	Zn^{2+} concentration (mg L^{-1})	Cu^{2+} concentration (μg L^{-1})	Corrosion rate (μm per year)
Zn	10.83	−1.22	3.13 ± 0.58	—	270.72 ± 9.76
Zn-0.4Cu	6.78	−1.17	1.62 ± 0.49	14.31 ± 2.97	186.34 ± 8.63

Table 2 Fitting parameters of the equivalent circuits

Samples	R_s (Ω cm^2)	*R*1 (kΩ cm^2)	CPE1 (10^{-6} Ω^{-1} cm^{-2} s^{n1})	R_{ct} (kΩ cm^2)	CPE2 (10^{-6} Ω^{-1} cm^{-2} s^{n2})	*W* (Ω^{-1} cm^{-2} s$^{0.5}$)
Zn	63.5	0.4	2.0	1.9	2.3	1.3
Zn-0.4Cu	59.7	2.3	2.1	3.3	7.9	22.3

carbonates. The O 1s spectrum displayed two binding energy peaks at 531 and 532 eV, associated with metal carbonates and metal hydroxides, respectively. Additionally, the fine spectra of phosphorus (P) and calcium (Ca) confirmed the presence of calcium phosphate ($Ca_3(PO_4)_2$) and calcium carbonate ($CaCO_3$) compounds within the corrosion product layer, while the Zn spectrum indicated the presence of zinc oxide (ZnO). For the Zn-0.4Cu alloy, the types of compounds present in the corrosion products were similar, although their relative concentrations differed. Notably, no peaks were detected in the Cu spectrum, indicating that no compounds containing copper were present in the corrosion layer. Table 3 summarizes the contents of the various elements in the corrosion layers of the pure Zn and Zn-0.4Cu alloys.

Cytocompatibility

Bone marrow stem cells (BMSCs) and endothelial cells (ECs) were seeded in prepared extracts and cultured for 3 days. The cell proliferation was evaluated using a cell proliferation assay kit (CCK8 method). The results, shown in Fig. 8(a) and (b), indicated that the activity of BMSCs and ECs cultured with extracts from the both pure Zn and Zn-0.4Cu alloy exceeded 80%, closely resembling the activity of pure titanium (Ti) in the control group. Both the pure Zn and Zn-0.4Cu alloy exhibited

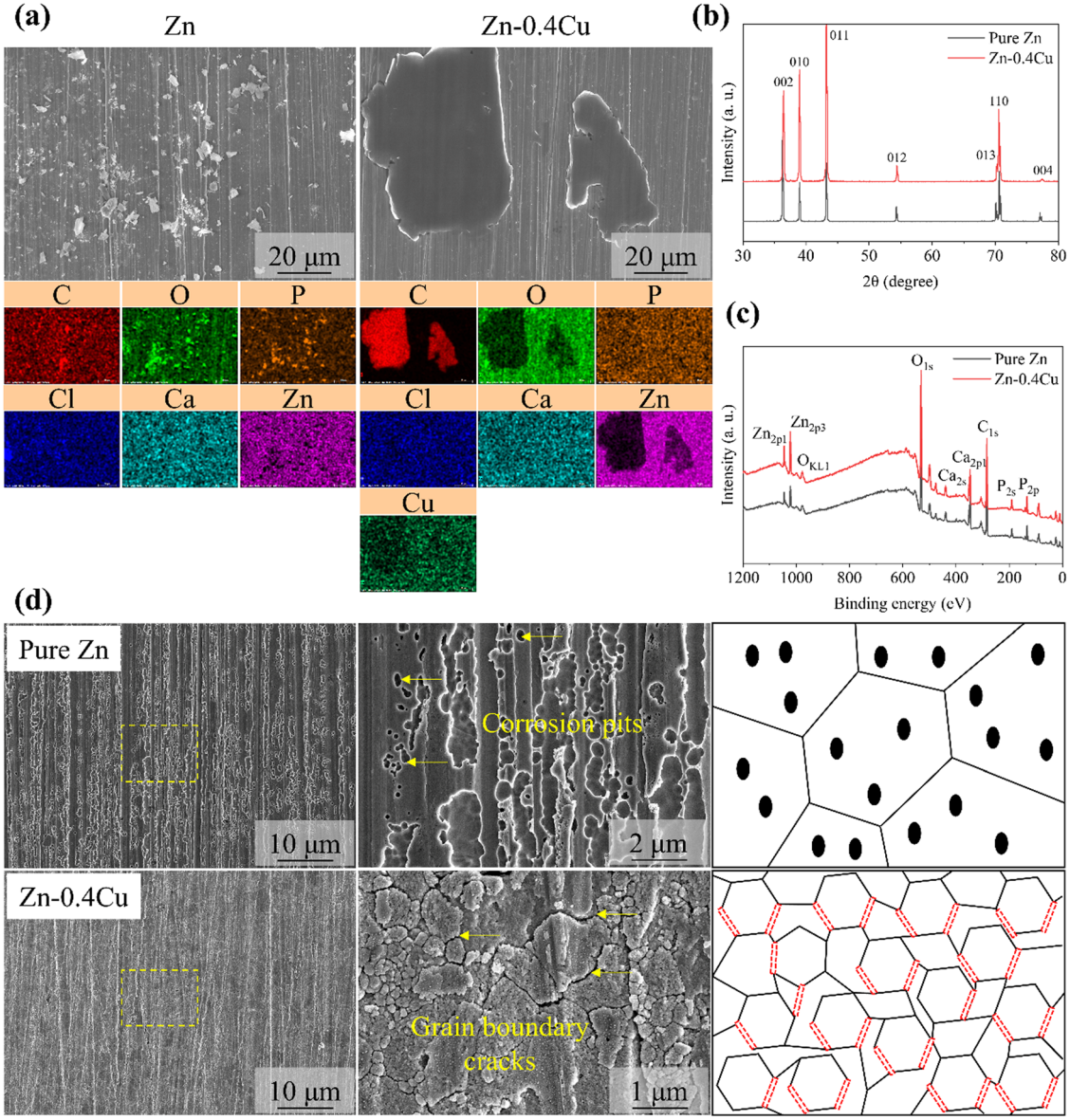

Fig. 6 Corrosion behaviors of the samples during immersion: (a) corrosion products and the corresponding elemental distributions. (b) XRD spectra. (c) XPS survey spectra. (d) Surface morphologies after removing the corrosion products and corrosion modes.

excellent biocompatibility, promoting the proliferation of BMSCs and ECs. To further analyze the effects of metallic ions on cell viability, the original extracts were analyzed by ICP-MS. The Zn^{2+} ion concentrations of the pure Zn extract and Zn-0.4Cu alloy extract were 133.3 and 93.5 μg L^{-1}, respectively. Moreover, the Cu^{2+} ion concentration in the Zn-0.4Cu alloy extract was 0.7 μg L^{-1}.

Furthermore, a live/dead cell double staining kit was employed to analyze the viability of the cells cultured in the extracts. Fig. 8(c) illustrates the live cells stained green and dead cells stained red. The results demonstrate that there were almost no dead cells, with the number of viable cells in the pure Zn and Zn-0.4Cu alloy groups being comparable to that of the pure Ti group. The live/dead staining results further confirmed that the extracts from the pure Zn and Zn-0.4Cu alloys were non-toxic to the proliferation of BMSCs and ECs, indicating their high safety profile.

Osteogenic properties

ALP staining and alizarin red S calcium nodule staining were used to characterize the contributing bone properties of the material, as shown in Fig. 9(a). As can be seen from the figure, the proportion of blue in the ALP staining image of the Zn-0.4Cu alloy group was higher, which indicates that the alloy had a better ability to promote bone growth in the early stage. In the images stained with alizarin red, the red calcium nodules in the Zn-0.4Cu alloy group were significantly higher than those in the pure Zn group and the pure Ti group. The results of osteogenic induction staining showed that Zn-0.4Cu alloy had better bone-promoting properties. Fig. 9(b) shows the expressions of four

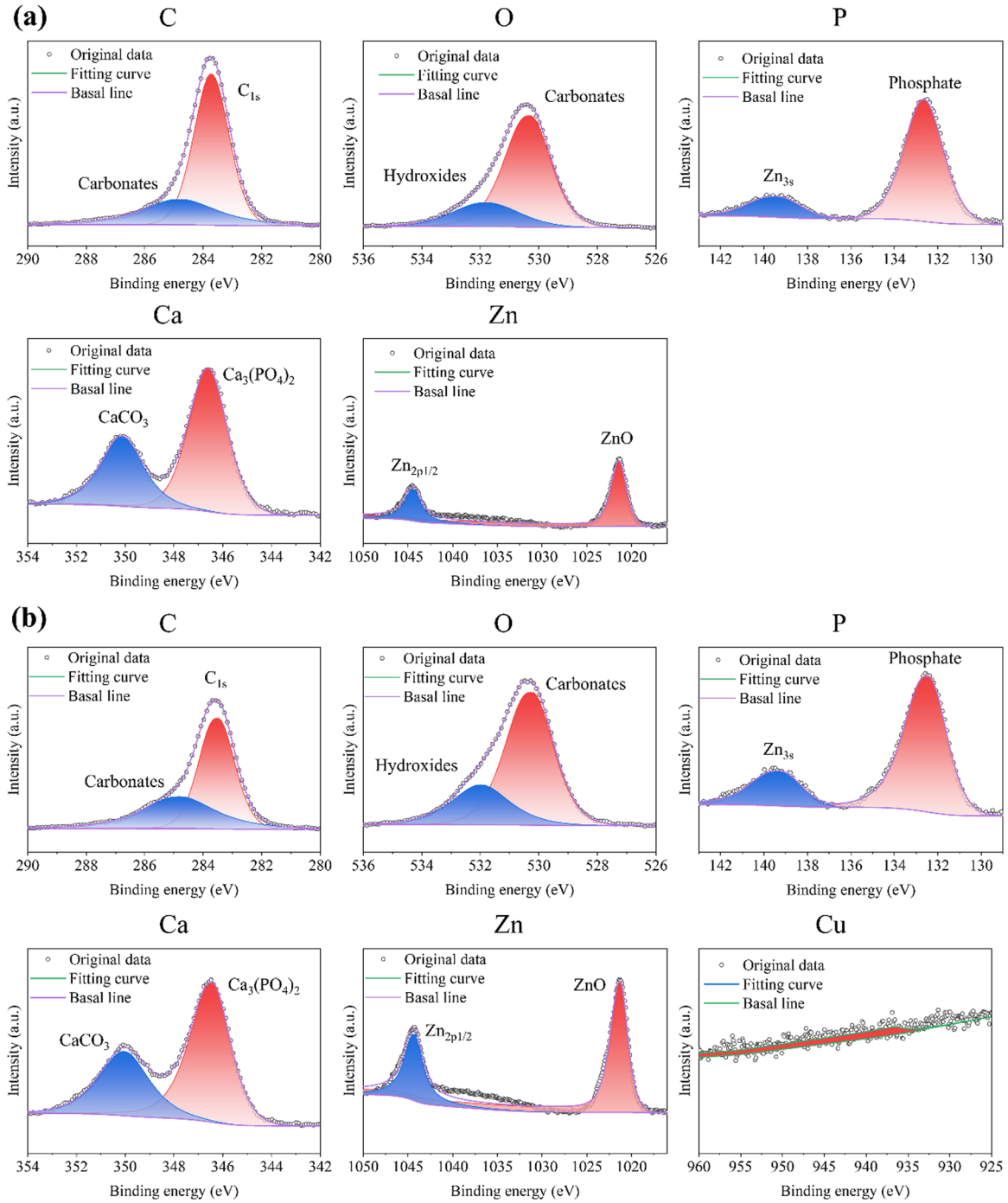

Fig. 7 Narrow spectra of the corrosion products: (a) pure Zn. (b) Zn–0.4Cu.

osteogenesis-related genes, namely ALP, COL-1, OPN, and Runx-2. For these four genes, the Zn-0.4Cu alloy group demonstrated higher expression levels than the pure Zn and pure Ti groups, and the expression levels of OPN and Runx-2 were especially higher than those in the other groups. The OPN expression level of the Zn-0.4Cu alloy group (3.79 ± 0.84) was nearly twice that of the pure Zn group (1.78 ± 0.41) under the culture condition of 50% extract; while the expression level of Runx-2 in the Zn-0.4Cu alloy group (4.14 ± 0.43) was nearly twice that of the pure Zn group (2.25 ± 0.32).

Table 3 Atomic concentrations of elements detected by XPS

	Atomic concentration (at%)					
Samples	C_{1s}	O_{1s}	P_{2p}	Ca_{2p}	Zn_{2p}	Cu_{2p}
Pure Zn	55.44	27.31	8.87	6.01	2.36	—
Zn-0.4Cu	45.43	33.08	10.55	5.96	4.74	0.24

Immunofluorescence staining (Fig. 9(c)) revealed that Zn-0.4Cu promoted higher Runx2 and higher OPN expressions (red) compared to pure Zn, with more intense fluorescence

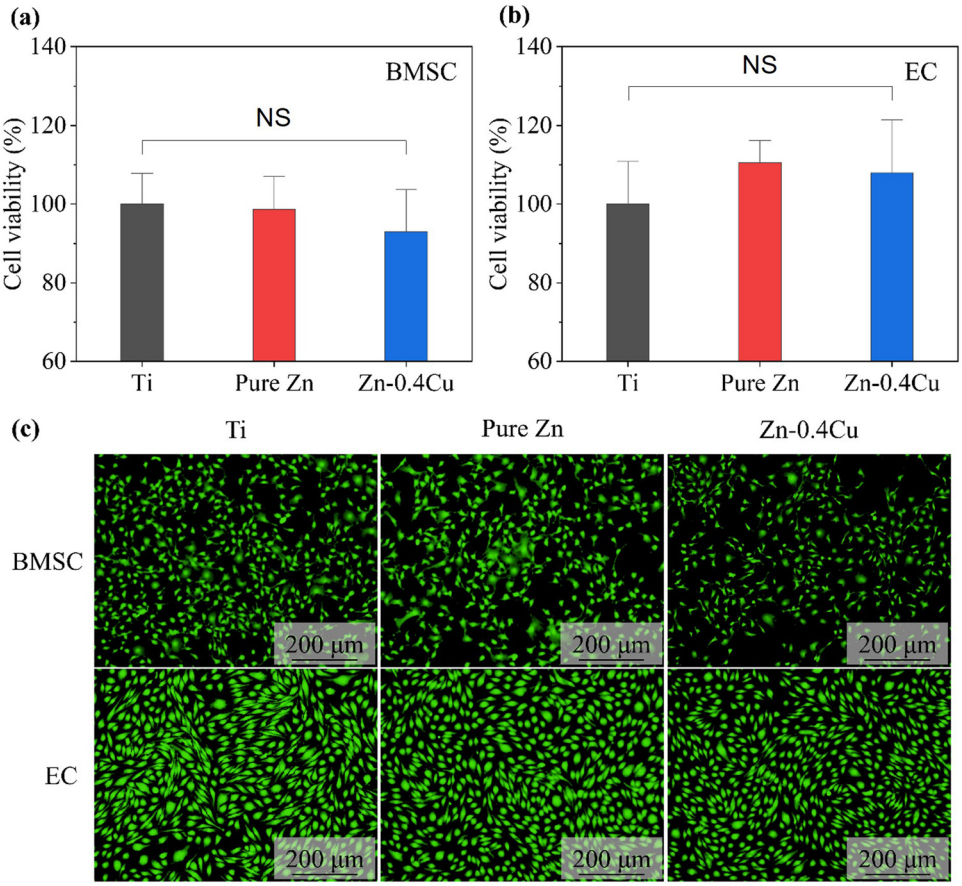

Fig. 8 Cytocompatibility of samples: cell viability of (a) BMSCs, (b) ECs. (c) Live/dead staining images.

signals, indicating increased osteogenic differentiation. DAPI staining (blue) showed well-distributed nuclei, while FITC staining (green) highlighted the presence of elongated and well-spread cytoskeletons in the Zn-0.4Cu-treated cells. These findings indicate that Zn-0.4Cu is a promising material for bone-implant applications.

Antibacterial properties

Fig. 10 illustrates the antimicrobial effects of the pure Zn and Zn–Cu alloys against *S. aureus* and *E. coli*. A substantial number of bacteria were observed evenly distributed in the inert metal titanium (Ti) group, while the numbers of bacteria were significantly decreased in the pure Zn and Zn-0.4Cu alloy groups. Notably, the *E. coli* count in the Zn-0.4Cu alloy group was markedly low, indicating that both the pure Zn and Zn-0.4Cu alloy possessed superior antimicrobial properties.

Crystal violet staining, a widely used chemical method for quantitatively assessing bacterial biofilms, stains live and dead cells as well as components within the biofilm matrix. This makes it particularly effective for quantifying total biofilm biomass in various assays. The results from the crystal violet staining experiments performed herein further corroborated that the Zn–Cu alloy exhibited enhanced antibacterial effects, especially against *E. coli*.

Discussion

Effects of the grain size on the mechanical behaviors

The average grain size of the Zn–0.4Cu alloy (2.15 μm) was significantly smaller than that of pure Zn (17.36 μm) after ECAP processing. According to the Hall–Petch relationship $\Delta\sigma = kd^{-\frac{1}{2}}$, grain refinement typically leads to an increase in yield strength.[33] However, the yield strength increment (~58 MPa) in the Zn-0.4Cu alloy was far lower than the strength contribution from grain boundary strengthening (~100 MPa). This indicated that grain boundary softening occurred in the Zn-0.4Cu alloy. In general, grain boundary hardening occurs at low temperature ($T < 0.3T_m$, where T_m is melting temperature), while grain boundary softening occurs at high temperature ($T > 0.5T_m$).[34] It can be inferred that the testing temperature (298 K) was 0.43 T_m owing to the low melting point of Zn (692 K). Thus, the mechanical behaviors of the Zn-0.4Cu alloy at room temperature should be described by a creep mechanism: $\dot{\varepsilon} = \frac{ADGb}{kT}\left(\frac{\sigma}{G}\right)^n\left(\frac{b}{d}\right)^p$, where D, G, b, T, σ and d are the diffusion coefficient, shear modulus, Burgers vector, temperature, stress and grain size, respectively, and A, k, p, and n are constants.[35] Among these constants, the p value is significantly affected by the creep mechanism. For dislocation viscous slip or climb within Zn grains, the p value is close to

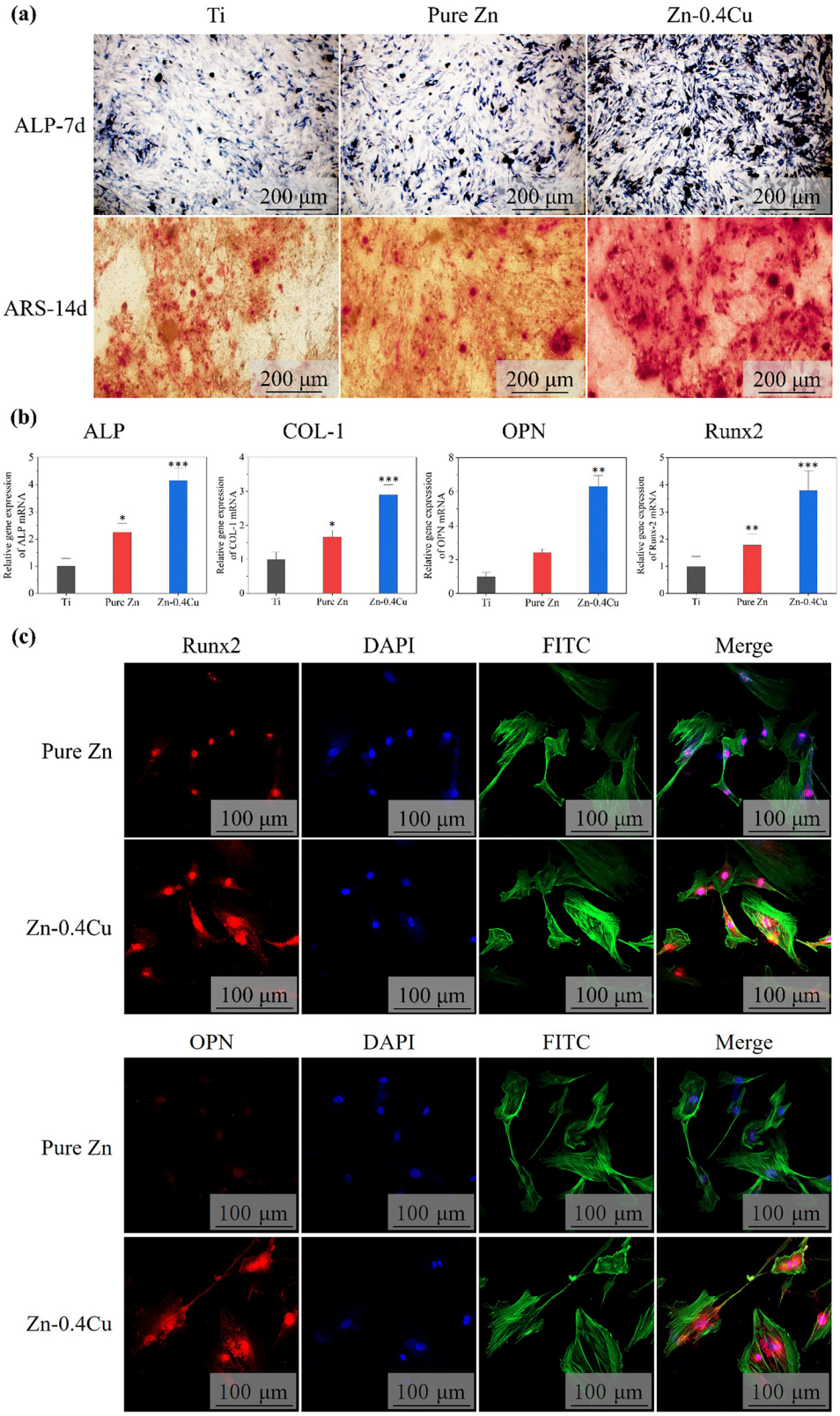

Fig. 9 Osteogenic properties of the samples: (a) ALP and ARS staining images. (b) Relative gene expression of various mRNA. (c) Immunofluorescence staining.

zero, indicating a weaker grain boundary strengthening.[36] Grain boundary sliding leads to a positive p value, resulting in a reduction of stress with decreasing grain size.[37] Moreover, the plate-shape precipitated play a positive role in improving the strength of the Zn-0.4Cu alloy. Compared to the Zn–0.5Cu alloy with a higher Cu content, the density of precipitates in the

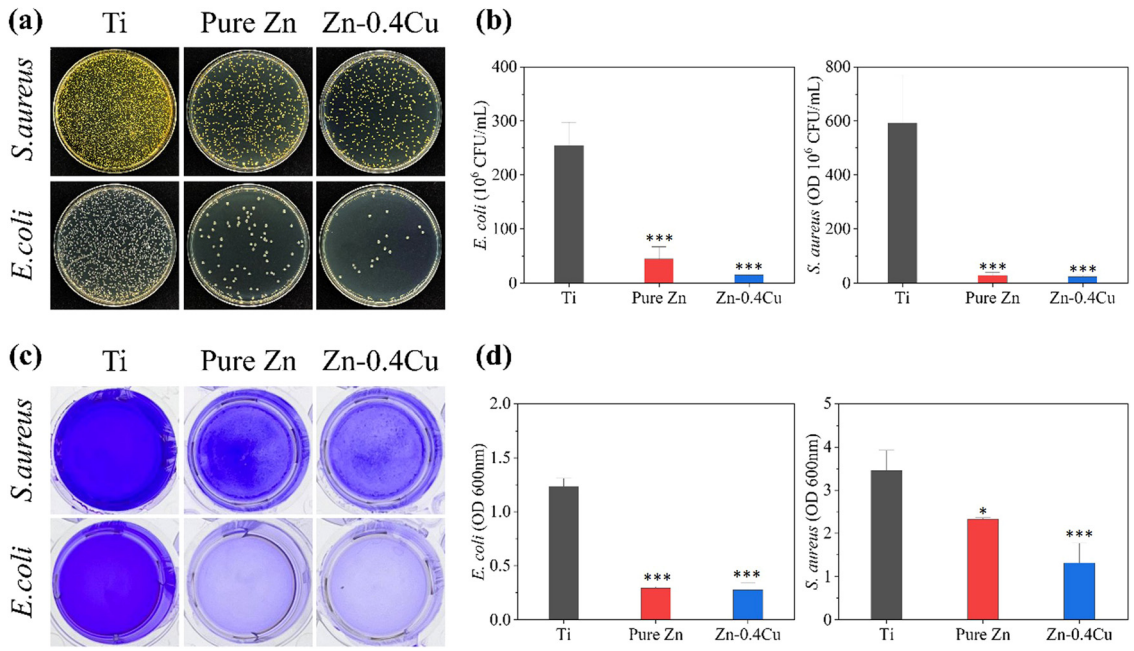

Fig. 10 Antibacterial properties of pure Zn and Zn-0.4Cu: (a) photos of the spread plate method. (b) Colony counts of *E. coli* and *S. aureus* bacteria on the sample surfaces. (c) Photos of the crystal violet method. (d) Quantitative results of the crystal violet method.

Zn-0.4Cu alloy was lower. This resulted in a UTS of 130 MPa, which was lower than the 179 MPa of the Zn–0.5Cu alloy.[26] That is, grain refinement increased the grain boundary density, but the contribution of the grain boundary strengthening to the Zn-0.4Cu alloy was limited. The plate-shaped precipitates are obstacles to dislocation motion, thereby leading to the improvement of strength.

Furthermore, the elongation of the Zn-0.4Cu alloy was significantly greater than that of the pure Zn, exhibiting superplasticity at room temperature. This difference in mechanical properties could be attributed to a change in the deformation mode. The effects of the grain sizes on the deformation modes have been reported in pure Mg, which has a higher elongation at a fine grain level.[38,39] The deformation of pure Zn with large grain sizes was dominated by twinning and dislocation slips. Independent slipping systems are insufficient in hexagonal close-packed (HCP) crystals, and then twining becomes a vital deformation mode.[40] With increasing strain, the proportion of deformation twins in coarse grains increased significantly for pure Zn, resulting in an improvement in the density of twin grain boundaries (as shown in Fig. 4(e)). On the one hand, the increase in the fraction of deformation twins reduces the average free path of the dislocation motion within grains, which is conducive to improving the strength;[41,42] while on the other hand, the twins promote grain refinement through a twinning-induced DRX mechanism, so as to achieve the goal of improving the strength.[3,4,43,44] The tensile curve indicates that pure Zn had a prolonged work-hardening stage during plastic deformation. This work hardening arose from the presence of deformation twins during tension.

The IPF map of the Zn-0.4Cu alloy clearly revealed a significant number of elongated grains, along with a smaller number of dynamically recrystallized grains characterized by low GOS values. Grain reference orientation deviation (GROD) was applied to quantify the misorientation between the position and the mean orientation of the grains. In pure Zn, most the grains lacked distinct deflection axes, indicating that their deformation was primarily due to twin deformation or simultaneous multiple dislocation activities. Conversely, the grains in the Zn-0.4Cu alloy predominantly exhibited deflections along the ⟨0001⟩ and ⟨11−20⟩ axes, suggesting that basal and cone dislocation slip governed the tensile deformation, as illustrated in Fig. 11(a). This dislocation slip further increased the grain's length-to-width ratio from 2.1 to 2.7. Additionally, the GROD-angle reflects the orientation difference between any point within the grain and the average grain orientation; whereby higher values indicate greater deformation due to dislocation slip. The results in Fig. 11(d) show that the GROD-angle value for the Zn-0.4Cu alloy was significantly higher than that of pure Zn.

In addition to twin deformation and dislocation slip, the high elongation of the Zn-0.4Cu alloy at room temperature may also be attributed to grain boundary slip. Recent studies have demonstrated that the tensile testing of superplastic Zn–Cu alloys at room temperature across various strain rates (10^{-4} to 10^{-3} s^{-1}) involve grain boundary slip. In summary, while pure Zn primarily deformed through twin crystals during tensile testing, the Zn-0.4Cu alloy was chiefly influenced by dislocation slip and grain boundary slip. This divergence in deformation mechanisms leads to a substantial difference in their mechanical properties.

Effects of the grain size on the corrosion behavior

Corrosion significantly impacts the biocompatibility and long-term clinical viability of medical implants, making the

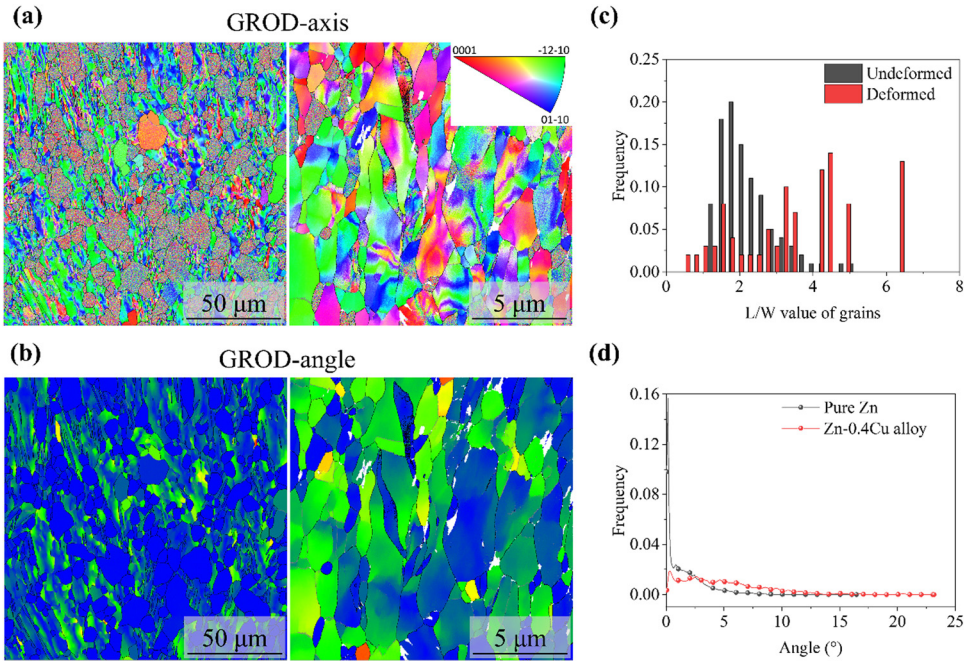

Fig. 11 Microstructural analysis of a deformed specimen: (a) GROD axis. (b) GROD angle. (c) Ratio of the length and width of grains in the Zn-0.4Cu alloy before and after fracture. (d) FROD angle distributions of the fractured pure Zn and Zn-0.4Cu alloy.

evaluation of the corrosion behavior of biodegradable metals essential for their biomedical applicability. Previous studies have indicated that, in NaOH solution, reducing the grain size of zinc to the nanoscale results in a decreased corrosion rate due to the reduced kinetics of the anodic and cathodic reactions.[45] However, in NaCl solution, grain refinement in Zn-containing alloys leads to increased corrosion rates because the higher density of grain boundaries provides more initiation points for corrosion, especially when impurities segregate at these boundaries.[46] The electrochemical and immersion experiments herein demonstrated that the Zn-0.4Cu alloy exhibited superior corrosion resistance compared to pure Zn. The polarization curve indicated that this reduced corrosion rate could be attributed to the passivation process occurring at the anode of the Zn-0.4Cu alloy, wherein an oxide layer formed on the metal surface, preventing further corrosion.

The primary microstructural difference between the pure Zn and the Zn-0.4Cu alloy was the grain size, although a small number of nanoscale precipitates were present. Analysis of the corrosion morphology of pure Zn revealed numerous corrosion pits, indicating that its primary corrosion mode was pitting. In contrast, the Zn-0.4Cu alloy predominantly experienced grain boundary corrosion. The EBSD results revealed that the high angle grain boundary density of pure Zn was 1.0×10^{-5} m^{-1}, while that of the Zn-0.4Cu alloy was 9.6×10^{-5} m^{-1}. Generally, grain boundaries possess a higher energy and increased chemical reactivity compared to the matrix material, leading to a higher surface activity due to enhanced electron activity and diffusion. This results in the rapid formation of a uniform and dense protective oxide layer.

TEM analysis further showed a bilayer of copper enrichment at the grain boundaries of the Zn-0.4Cu alloy. This enrichment can lead to local galvanic corrosion near the grain boundaries upon contact with corrosive solutions, thereby accelerating grain boundary corrosion. Systematic studies on the effect of the grain size on the corrosion rates in various metals have suggested that when the corrosion current density is below 10 μA cm^{-2}, smaller grain sizes can promote the formation of a dense oxide film on the metal surface, enhancing corrosion resistance.[47] In this study, the corrosion current density for pure Zn was 10.83 μA cm^{-2}, whereas that for the Zn-0.4Cu alloy was 6.87 μA cm^{-2}, further supporting the formation of a dense oxide film during the corrosion process of the Zn-0.4Cu alloy. In summary, the higher corrosion rate observed in pure Zn compared to in the Zn-0.4Cu alloy was attributed to a shift in the corrosion mode from pitting to grain boundary corrosion. This transition was primarily caused by the copper enrichment at grain boundaries, leading to the formation of a galvanic cell structure that accelerates grain boundary corrosion. The change in corrosion mode promoted the formation of a stable oxide film on the surface of the Zn-0.4Cu alloy, effectively inhibiting further corrosion of the alloy.

In vitro biocompatibility and osteogenic properties

The ionic concentration in solution plays a crucial role in determining the osmotic pressure of cells, leading to their dose-dependent tolerance to metal ions.[48] For example, He *et al.* observed a sharp decline in the activity of MC3T3-E1 cells with Zn ion concentrations exceeding 0.3 mM.[49] Similarly, Xiong *et al.* found that BMSCs activity increased with Zn ion concentrations ranging between 10.92 and 27.15 μM but began to decrease when the concentration reached 128.58 μM.[50] In our study, the Zn-0.4Cu alloy exhibited a lower corrosion rate

than pure Zn, resulting in a higher Zn ion concentration in the pure Zn group compared to the Zn-0.4Cu alloy group. The Zn-0.4Cu alloy solution also contained a small amount of Cu ions, but the concentration was much lower than that of Zn ions. Notably, BMSCs and ECs cultured in one-fold diluted pure Zn extracts showed higher activity than those in the Zn-0.4Cu alloy extracts. Then, as the extract concentration was diluted, the ionic concentration decreased to a level more conducive to cell growth and proliferation, significantly enhancing cell viability.

The ALP results demonstrated the superior osteogenic properties of the Zn-0.4Cu alloy for BMSCs. This improvement could be attributed to the co-release of Zn^{2+} and Cu^{2+} ions. The PCR results showed that the expressions of osteogenic markers, such as OCN, COL-I, ALP, and RUNX-2, were promoted, corroborating previous studies.[51] The Zn^{2+} ions in the diluted extracts activated the typical MAPK pathway, leading to the promotion of BMSCs osteogenic differentiation through p38MAPK signaling and RUNX/OSX-regulated MAPK signaling pathways.[52] Additionally, Zn has been shown to benefit BMSCs' osteogenic activity by activating RUNX-2 *via* the cyclic adenosine monophosphate (cAMP)-protein kinase A (PKA)-cAMP response binding protein (CREB) signaling pathway.[53] Apart from Zn^{2+}, the effects of Cu^{2+} on bone metabolism regulation and bone regeneration are also significant. Previous studies found that Cu^{2+} facilitated the osteogenic differentiation of BMSCs by increasing ALP activity and the levels of OPN and OCN.[54] However, Cu^{2+} can also induce osteoblast injury by suppressing the TGF-1/Smad3 pathway.[55] In summary, the synergistic effect of Zn^{2+} and Cu^{2+} ions contributed to the enhanced osteogenic properties of the Zn-0.4Cu alloy.

Conclusions

In this experiment, pure Zn and Zn-0.4Cu alloys were subjected to ECAP at room temperature, followed by a comprehensive investigation of their microstructure, mechanical properties, corrosion behavior, biocompatibility, and antibacterial properties. After ECAP, the grain size of the Zn-0.4Cu alloy was refined to approximately 2 μm, significantly smaller than the 17 μm of pure Zn. Additionally, needle-like precipitates were identified within the Zn-0.4Cu alloy, exhibiting coherent interfaces with the surrounding matrix. Regarding the mechanical properties, the Zn-0.4Cu alloy demonstrated a slightly greater strength than the pure Zn, while its elongation was twice that of pure Zn. These differences were primarily due to the distinct deformation mechanisms; pure Zn primarily undergoes twinning, whereas the Zn-0.4Cu alloy predominantly experiences dislocation slip and grain boundary sliding. Corrosion tests revealed that the Zn–Cu alloy, with its finer grains, exhibited improved corrosion resistance compared to pure Zn. The corrosion mode of pure Zn was primarily characterized by pitting, whereas the Zn–Cu alloy experienced grain boundary corrosion. This grain boundary corrosion was attributed to the accumulation of copper near the grain boundaries, which accelerated corrosion through galvanic effects. Both the pure Zn and Zn–Cu alloys exhibited excellent biocompatibility with endothelial cells (ECs) and bone marrow stem cells (BMSCs). Notably, the osteogenic and antibacterial properties of the Zn–Cu alloy surpassed those of pure Zn, highlighting its potential for biomedical applications.

Author contributions

Haifeng Liang: conceptualization, project administration, methodology, data curation, writing – review & editing; Haoran Wu: methodology, resources, writing – original draft, funding acquisition; Delong Yin: visualization, writing – original draft, funding acquisition; Hui Yu: investigation, resources, data curation; Zhuoxuan He: investigation, visualization, writing – original draft; Wenqian Zhang: investigation, writing – original draft; Zerong Wang: investigation, visualization; Tuquan Zheng: investigation, visualization; Xiaochuan Li: conceptualization, supervision, data curation, writing – review & editing; Yu Cai: conceptualization, methodology, writing – review & editing; Guiyong Jiang: conceptualization, supervision, project administration, writing – review & editing.

Data availability

Data are available from the authors on request.

Conflicts of interest

There are no conflicts of interest to disclose.

Acknowledgements

This work was supported by the Plan for Enhancing Scientific Research in GMU (2024SRP124), the Startup Research Fund of the Henan Academy of Science (241817055), and the Natural Science Foundation of Henan (252300420460).

References

1 P. K. Bowen, J. Drelich and J. Goldman, Zinc exhibits ideal physiological corrosion behavior for bioabsorbable stents, *Adv. Mater.*, 2013, **25**(18), 2577–2582.
2 H. Yang, C. Wang, C. Liu, H. Chen, Y. Wu, J. Han, Z. Jia, W. Lin, D. Zhang, W. Li, W. Yuan, H. Guo, H. Li, G. Yang, D. Kong, D. Zhu, K. Takashima, L. Ruan, J. Nie, X. Li and Y. Zheng, Evolution of the degradation mechanism of pure zinc stent in the one-year study of rabbit abdominal aorta model, *Biomaterials*, 2017, **145**, 92–105.
3 S. Liu, D. Kent, H. Zhan, N. Doan, M. Dargusch and G. Wang, Dynamic recrystallization of pure zinc during high strain-rate compression at ambient temperature, *Mater. Sci. Eng., A*, 2020, **784**, 139325.
4 M. Chegini, S. M. Fatemi, N. Mollaei and W. Bednarczyk, The temperature dependence of cyclic dynamic recrystallization in as-extruded pure zinc, *J. Mater. Res. Technol.*, 2023, **26**, 9370–9379.

5 W. Bednarczyk, J. Kawałko, M. Wątroba and P. Bała, Achieving room temperature superplasticity in the Zn–0.5Cu alloy processed via equal channel angular pressing, *Mater. Sci. Eng., A*, 2018, **723**, 126–133.
6 W. Bednarczyk, M. Wątroba, J. Kawałko and P. Bała, Can zinc alloys be strengthened by grain refinement? A critical evaluation of the processing of low-alloyed binary zinc alloys using ECAP, *Mater. Sci. Eng., A*, 2019, **748**, 357–366.
7 W. Bednarczyk, M. Wątroba, J. Kawałko and P. Bała, Determination of room-temperature superplastic asymmetry and anisotropy of Zn-0.8Ag alloy processed by ECAP, *Mater. Sci. Eng., A*, 2019, **759**, 55–58.
8 P. Guo, F. Li, L. Yang, R. Bagheri, Q. Zhang, B. Q. Li, K. Cho, Z. Song, W. Sun and H. Liu, Ultra-fine-grained Zn-0.5Mn alloy processed by multi-pass hot extrusion: Grain refinement mechanism and room-temperature superplasticity, *Mater. Sci. Eng., A*, 2019, **748**, 262–266.
9 E. Mostaed, M. S. Ardakani, M. Sikora-Jasinska and J. W. Drelich, Precipitation induced room temperature superplasticity in Zn–Cu alloys, *Mater. Lett.*, 2019, **244**, 203–206.
10 P. Guo, X. Zhu, L. Yang, L. Deng, Q. Zhang, B. Q. Li, K. Cho, W. Sun, T. Ren and Z. Song, Ultrafine- and uniform-grained biodegradable Zn–0.5Mn alloy: Grain refinement mechanism, corrosion behavior, and biocompatibility *in vivo*, *Mater. Sci. Eng., C*, 2021, **118**, 111391.
11 J. Jiang, Y. Qian, H. Huang, J. Niu and G. Yuan, Biodegradable Zn–Cu–Mn alloy with suitable mechanical performance and in vitro degradation behavior as a promising candidate for vascular stents, *Biomater. Adv.*, 2022, **133**, 112652.
12 C. Zhou, X. Feng, Z. Shi, C. Song, X. Cui, J. Zhang, T. Li, E. S. Toft, J. Ge, L. Wang and H. Zhang, Research on elastic recoil and restoration of vessel pulsatility of Zn–Cu biodegradable coronary stents, *Biomed. Technol.*, 2020, **65**(2), 219–227.
13 Y. Shan, B. Qiao, S. Ouyang, C. Du, L. Zhao, G. Wang, J. Ye, Y. Xiong, Y. Wei, J. Song, J. She, J. Peng, X. Chen, F. Pan and N. Wen, Biodegradable Mg–Ca/Mg–Cu bilayer membranes with enhanced mechanical, osteogenesis and antibacterial performances for GBR applications, *J. Magnesium Alloys*, 2024, 792–809.
14 K. Chen, X. Gu, N. Zhang, L. Zhao, C. Huang, Y. Qin, Y. Cheng, Y. Zheng and Y. Fan, Corrosion behavior and mechanical integrity of Zn-based guided bone generation (GBR) membrane subjected to U-bending deformation, *Corros. Sci.*, 2024, **236**, 112272.
15 X.-M. Li, Z.-Z. Shi, A. Tuoliken, W. Gou, C.-H. Li and L.-N. Wang, Highly plastic Zn-0.3Ca alloy for guided bone regeneration membrane: Breaking the trade-off between antibacterial ability and biocompatibility, *Bioact. Mater.*, 2024, **42**, 550–572.
16 W. Zhang, P. Li, G. Shen, X. Mo, C. Zhou, D. Alexander, F. Rupp, J. Geis-Gerstorfer, H. Zhang and G. Wan, Appropriately adapted properties of hot-extruded Zn–0.5Cu–*x*Fe alloys aimed for biodegradable guided bone regeneration membrane application, *Bioact. Mater.*, 2021, **6**(4), 975–989.
17 H. Guo, D. Xia, Y. Zheng, Y. Zhu, Y. Liu and Y. Zhou, A pure zinc membrane with degradability and osteogenesis promotion for guided bone regeneration: *In vitro* and *in vivo* studies, *Acta Biomater.*, 2020, **106**, 396–409.
18 E. Mostaed, M. Sikora-Jasinska, J. W. Drelich and M. Vedani, Zinc-based alloys for degradable vascular stent applications, *Acta Biomater.*, 2018, **71**, 1–23.
19 J. Venezuela and M. S. Dargusch, The influence of alloying and fabrication techniques on the mechanical properties, biodegradability and biocompatibility of zinc: A comprehensive review, *Acta Biomater.*, 2019, **87**, 1–40.
20 P. Li, W. Zhang, J. Dai, A. B. Xepapadeas, E. Schweizer, D. Alexander, L. Scheideler, C. Zhou, H. Zhang, G. Wan and J. Geis-Gerstorfer, Investigation of zinc–copper alloys as potential materials for craniomaxillofacial osteosynthesis implants, *Mater. Sci. Eng., C*, 2019, **103**, 109826.
21 G. Bao, K. Wang, L. Yang, J. He, B. He, X. Xu and Y. Zheng, Feasibility evaluation of a Zn–Cu alloy for intrauterine devices: *In vitro* and *in vivo* studies, *Acta Biomater.*, 2022, **142**, 374–387.
22 M. Bost, S. Houdart, M. Oberli, E. Kalonji, J.-F. Huneau and I. Margaritis, Dietary copper and human health: Current evidence and unresolved issues, *J. Trace Elem. Med. Biol.*, 2016, **35**, 107–115.
23 R. Z. Valiev and T. G. Langdon, Principles of equal-channel angular pressing as a processing tool for grain refinement, *Prog. Mater. Sci.*, 2006, **51**(7), 881–981.
24 K. Ren, K. Zhang, Y. Zhang, J. Ju, K. Yan, J. Jiang, A. Ma, F. Xue, J. Bai and H. Liu, Effect of ECAP temperature on formation of triple heterogeneous microstructure and mechanical properties of Zn–1Cu alloy, *Mater. Sci. Eng., A*, 2021, **826**, 141990.
25 Z. Xu, H. Liu, K. Ren, C. Sun, X. Zhuo, K. Yan, J. Ju, F. Xue, J. Bai and J. Jiang, Revealing the abnormal softening mechanisms of Zn–*x*Cu (x = 2, 3) wrought alloys by gradually increasing ECAP numbers, *Mater. Sci. Eng., A*, 2022, **856**, 143962.
26 L. Ye, C. Sun, X. Zhuo, H. Liu, J. Ju, F. Xue, J. Bai, J. Jiang and Y. Xin, Evolution of grain size and texture of Zn–0.5Cu ECAP alloy during annealing at 200 °C and its impact on mechanical properties, *J. Alloys Compd.*, 2022, **919**, 165871.
27 W. Zhang, X. Sun, D. Liu, G. Liang and J. Gao, Microstructure and properties of biodegradable Zn–0.8Mn–0.5Cu–0.2Sr alloys processed by ECAP, *Mater. Today Commun.*, 2024, **39**, 108630.
28 C. Ji, A. Ma, J. Jiang, H. Wu, H. Liu, S. Guo and Y. Yuan, Regulating mechanical properties and degradation behavior of biodegradable Zn–0.6Mg alloy *via* ECAP plus cold rolling, *J. Alloys Compd.*, 2023, **937**, 168487.
29 H. Lee, I. Lee, X. Xu, T. Omori and R. Kainuma, Revisiting the Phase Equilibria in the Cu–Zn Binary System, *J. Phase Equilib. Diffus.*, 2024, **45**(3), 304–317.
30 H. R. Bakhsheshi-Rad, E. Hamzah, H. T. Low, M. H. Cho, M. Kasiri-Asgarani, S. Farahany, A. Mostafa and M. Medraj, Thermal Characteristics, Mechanical Properties, *In Vitro* Degradation and Cytotoxicity of Novel Biodegradable Zn–Al–Mg and Zn–Al–Mg–xBi Alloys, *Acta Metall. Sin.*, 2017, **30**(3), 201–211.

31 H. R. Bakhsheshi-Rad, E. Hamzah, H. T. Low, M. Kasiri-Asgarani, S. Farahany, E. Akbari and M. H. Cho, Fabrication of biodegradable Zn–Al–Mg alloy: Mechanical properties, corrosion behavior, cytotoxicity and antibacterial activities, *Mater. Sci. Eng., C*, 2017, **73**, 215–219.

32 M. Cao, Z. Xue, Z.-Y. Lv, J.-L. Sun, Z.-Z. Shi and L.-N. Wang, 300 MPa grade highly ductile biodegradable Zn–2Cu–(0.2–0.8)Li alloys with novel ternary phases, *J. Mater. Sci. Technol.*, 2023, **157**, 234–245.

33 N. Hansen, Hall–Petch relation and boundary strengthening, *Scr. Mater.*, 2004, **51**(8), 801–806.

34 R. B. Figueiredo, M. Kawasaki and T. G. Langdon, Seventy years of Hall-Petch, ninety years of superplasticity and a generalized approach to the effect of grain size on flow stress, *Prog. Mater. Sci.*, 2023, **137**, 101131.

35 T. G. Langdon and F. A. Mohamed, A new type of deformation mechanism map for high-temperature creep, *Mater. Sci. Eng.*, 1978, **32**(2), 103–112.

36 J. Weertman, Steady-State Creep through Dislocation Climb, *J. Appl. Phys.*, 1957, **28**(3), 362–364.

37 T. G. Langdon, Grain boundary sliding revisited: Developments in sliding over four decades, *J. Mater. Sci.*, 2006, **41**(3), 597–609.

38 Z. Zeng, M. Zhou, P. Lynch, F. Mompiou, Q. Gu, M. Esmaily, Y. Yan, Y. Qiu, S. Xu, H. Fujii, C. Davies, J.-F. Nie and N. Birbilis, Deformation modes during room temperature tension of fine-grained pure magnesium, *Acta Mater.*, 2021, **206**, 116648.

39 R. Zheng, J.-P. Du, S. Gao, H. Somekawa, S. Ogata and N. Tsuji, Transition of dominant deformation mode in bulk polycrystalline pure Mg by ultra-grain refinement down to sub-micrometer, *Acta Mater.*, 2020, **198**, 35–46.

40 S. Liu, D. Kent, N. Doan, M. Dargusch and G. Wang, Effects of deformation twinning on the mechanical properties of biodegradable Zn–Mg alloys, *Bioact Mater.*, 2019, **4**(1), 8–16.

41 C. Wagner and G. Laplanche, Effect of grain size on critical twinning stress and work hardening behavior in the equiatomic CrMnFeCoNi high-entropy alloy, *Int. J. Plast.*, 2023, **166**, 103651.

42 G. Tsukamoto, T. Kunieda, M. Mitsuhara and H. Nakashima, Effect of twinning deformation on work hardening in commercially pure titanium, *Mater. Sci. Eng., A*, 2022, **840**, 142907.

43 S. Liu, D. Kent, H. Zhan, N. Doan, C. Wang, S. Yu, M. Dargusch and G. Wang, Influence of strain rate and crystallographic orientation on dynamic recrystallization of pure Zn during room-temperature compression, *J. Mater. Sci. Technol.*, 2021, **86**, 237–250.

44 G. Dirras, J. Gubicza, H. Couque, A. Ouarem and P. Jenei, Mechanical behaviour and underlying deformation mechanisms in coarse- and ultrafine-grained Zn over a wide range of strain rates, *Mater. Sci. Eng., A*, 2013, **564**, 273–283.

45 K. M. S. Youssef, C. C. Koch and P. S. Fedkiw, Improved corrosion behavior of nanocrystalline zinc produced by pulse-current electrodeposition, *Corros. Sci.*, 2004, **46**(1), 51–64.

46 M. C. Li, L. L. Jiang, W. Q. Zhang, Y. H. Qian, S. Z. Luo and J. N. Shen, Electrochemical corrosion behavior of nanocrystalline zinc coatings in 3.5% NaCl solutions, *J. Solid State Electrochem.*, 2007, **11**(9), 1319–1325.

47 K. D. Ralston, N. Birbilis and C. H. J. Davies, Revealing the relationship between grain size and corrosion rate of metals, *Scr. Mater.*, 2010, **63**(12), 1201–1204.

48 E. J. Calabrese, G. Dhawan, R. Kapoor, E. Agathokleous and V. Calabrese, Hormesis: Wound healing and keratinocytes, *Pharmacol. Res.*, 2022, **183**, 106393.

49 J. He, J. Fang, P. Wei, Y. Li, H. Guo, Q. Mei and F. Ren, Cancellous bone-like porous Fe@Zn scaffolds with core–shell-structured skeletons for biodegradable bone implants, *Acta Biomater.*, 2021, **121**, 665–681.

50 Z. Chen, W. Zhang, M. Wang, L. J. Backman and J. Chen, Effects of Zinc, Magnesium, and Iron Ions on Bone Tissue Engineering, *ACS Biomater. Sci. Eng.*, 2022, **8**(6), 2321–2335.

51 Y. Luo, H. Liu, Y. Zhang, Y. Liu, S. Liu, X. Liu and E. Luo, Metal ions: the unfading stars of bone regeneration-from bone metabolism regulation to biomaterial applications, *Biomater. Sci.*, 2023, **11**(22), 7268–7295.

52 Z. Wang, Q. Liu, C. Liu, W. Tan, M. Tang, X. Zhou, T. Sun and Y. Deng, Mg(2+) in β-TCP/Mg–Zn composite enhances the differentiation of human bone marrow stromal cells into osteoblasts through MAPK-regulated Runx2/Osx, *J. Cell. Physiol.*, 2020, **235**(6), 5182–5191.

53 K. H. Park, Y. Choi, D. S. Yoon, K.-M. Lee, D. Kim and J. W. Lee, Zinc Promotes Osteoblast Differentiation in Human Mesenchymal Stem Cells Via Activation of the cAMP-PKA-CREB Signaling Pathway, *Stem Cells Dev.*, 2018, **27**(16), 1125–1135.

54 L.-j Wang, X.-h Ni, F. Zhang, Z. Peng, F.-x Yu, L.-b Zhang, B. Li, Y. Jiao, Y.-k Li, B. Yang, X.-y Zhu and Q.-m Zhao, Osteoblast Response to Copper-Doped Microporous Coatings on Titanium for Improved Bone Integration, *Nanoscale Res. Lett.*, 2021, **16**(1), 146.

55 Y. Qi, H. Wang, X. Chen and Y. Zhu, The role of TGF-β1/Smad3 signaling pathway and oxidative stress in the inhibition of osteoblast mineralization by copper chloride, *Environ. Toxicol. Pharmacol.*, 2021, **84**, 103613.